ELECTRONIC SUPPLEMENTARY INFORMATION

Self-assembly of lobed particles into amorphous and crystalline porous structures

Sanjib Paul and Harish Vashisth*

Department of Chemical Engineering, University of New Hampshire, 33 Academic Way, Durham, NH 03824, USA

* Corresponding author; Email: harish.vashisth@unh.edu

MODELS AND METHODS

A. Interaction Potentials

In all simulations, the non-bonded interactions between the lobes are attractive and have been modeled by the Lennard-Jones potential,

$$V_{\mathrm{LJ}}(r) = 4\epsilon\left[\left(\frac{\sigma_L}{r}\right)^{12} - \left(\frac{\sigma_L}{r}\right)^{6}\right] \tag{S1}$$

where r is the distance between two lobes, ϵ is the energy well depth, and σ_L is the diameter of each lobe. The interactions between two seed particles and between a seed and a lobe are repulsive and have been modeled by surface-shifted Lennard-Jones potential (SSLJ) implemented in HOOMD-Blue. The functional form of the SSLJ potential acting between the particle i and the particle j is

$$V_{\mathrm{SSLJ}}(r) = \begin{cases} 4\epsilon_{ij}\left[\left(\frac{\sigma}{r-\Delta}\right)^{12} - \left(\frac{\sigma}{r-\Delta}\right)^{6}\right], & \text{when } r < r_{cut} + \Delta \\ 0, & \text{when } r \geq r_{cut} + \Delta \end{cases} \tag{S2}$$

where ϵ_{ij} is the energy well depth for the i-j pair and $\Delta = (\sigma_i + \sigma_j)/2 - 1$, where σ_i and σ_j are the diameters of the particle i and j, respectively.

B. Units and Parameters

All bonds and angles present in the lobed particles have been modeled by harmonic potentials and their corresponding force constants have been adjusted to retain the shape of each particle during simulations. In all simulations, we have used reduced units where the diameter of the lobe (σ_L), the mass of the lobe (m_L), and the depth of the potential well for the pair of seeds (ϵ_{CC}) have been used as the units of length, mass, and energy, respectively. The diameter of each lobe (σ_L) is 1 and the diameter of each seed (σ_C) is 2 for each building block. The masses of the lobes (m_L) and the seeds (m_C) were set to 1. The potential depths for the C-L pairs (ϵ_{CL}) and for the L-L pairs (ϵ_{LL}) have been fixed at 1 and 3, respectively. The interactions between the lobes are short-ranged and modeled via a cut-off distance which is equal to $3\sigma_L$. The σ values in the SSLJ potential are 2.0 and 1.5 for the seed-seed pairs and seed-lobe pairs, respectively.

The reduced temperature in simulations is described as $T^* = k_BT/\epsilon_{CC}$. We have gradually tuned the parameter $\tilde{\epsilon}_{LL}$ (ϵ_{LL}/k_BT) and observed its effect on the self-assembly. The $\tilde{\epsilon}_{LL}$ values employed in this work are 3.0, 3.8, 4.3, 5.0, 6.0 and 7.5. The corresponding T^* values are 1.0, 0.8, 0.7, 0.6, 0.5 and 0.4. We used the Langevin thermostat to maintain the temperature in all simulations. We carried out 6 simulations (one per $\tilde{\epsilon}_{LL}$ value) for each of the 7 types of lobed particles (overall 42 simulations) using a time step of 0.005, where each simulation was carried out for 1×10^8 steps to ensure that the potential energies are converged (Fig. S1) and the self-assembled structures produced are at equilibrium. In each direction, the length of the cubic simulation domain was 176 σ_L for all simulations and each simulation domain contained 21296 lobed particles of each type. The volume fraction, ϕ, of the lobed particles in the simulation domain vary from 0.02 to 0.03 depending on the number of lobes attached to the seed, where $\phi = NV/V_0$; N is the number of lobed particles present in the simulation domain, V_0 is the total volume of the simulation domain, and V is the volume of a lobed particle given as $V = V_C + N_LV_L$, where V_C is the the volume of the seed, N_L is the number of lobes attached to the central seed, and V_L is the volume of a lobe. We also carried out 12 additional simulations (3 each for lobed particles with the dumbbell, trigonal planar, square planar and trigonal bipyramid shapes) at different densities by varying ϕ between 0.01 and 0.11. In these simulations, the volumes of simulation domains were changed by varying the dimensions between 96 σ_L and 264 σ_L while keeping the same number of lobed particles. The results from these simulations are shown in Figs. S8, S9, and S10.

C. Radial Distribution Function

For the pair of seeds, the radial distribution function, g(r) at a distance r with respect to the reference particle is calculated using the following equation

$$g(\mathrm{r}) = \frac{\rho(\mathrm{r})}{\rho_o}, \tag{S3}$$

where ρ(r) is the number density at a distance r from a reference particle and ρ_o is the bulk density. ρ(r) was calculated by counting the number of particles present in a bin of width dr at a distance r with respect to the reference particle and then dividing that number by the volume of the bin.

D. Pore Volume Calculations

To calculate the pore volume, we used the largest possible cuboids extracted from self-assembled structures (Fig. S7). In all pore volume calculations, we used a probe radius of $\frac{1}{2}\sigma_L$.

E. Characterization of Self-assembled Clusters

We used the depth first search algorithm to find the number of clusters and the number of building blocks present in each cluster (Fig. S9). To determine whether a pair of building blocks belong to the same cluster, we used a cut-off distance equal to the distance at which the first minimum in the radial distribution function appears.

TABLES AND FIGURES

TABLE S1 Occurrence of self-assembly in different systems. ✓ indicates that the self-assembly occurs and × indicates that the self-assembly does not occur. We have also included the values of the reduced temperature, $T^*=k_BT/\epsilon_{CC}$, corresponding to each $\tilde{\epsilon}_{LL}$.

$\tilde{\epsilon_{LL}}$	T^*	S_1^{SM}	S_2^{DB}	S_3^{TP}	S_4^{SP}	S_4^{TH}	S_5^{TBP}	S_6^{OCT}
3.0	1.0	×	×	×	×	×	×	×
3.8	0.8	×	×	×	×	×	×	✓
4.3	0.7	×	×	×	×	×	✓	✓
5.0	0.6	×	×	×	✓	✓	✓	✓
6.0	0.5	×	×	✓	✓	✓	✓	✓
7.5	0.4	×	✓	✓	✓	✓	✓	✓

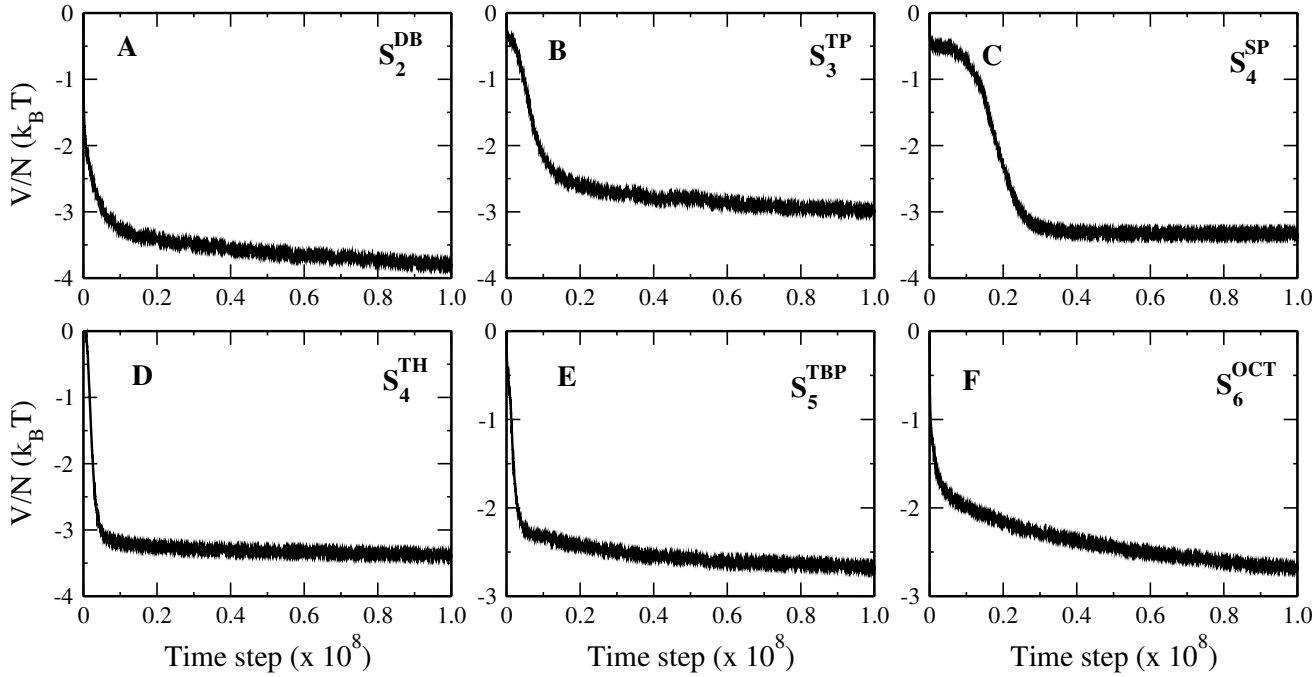

FIG. S1 Potential energy per particle (V/N) vs. simulation time for self-assemblies observed in particles with the following shapes: (A) dumbbell (S_2^{DB}) (at $\epsilon_{\tilde{LL}} = 7.5$), (B) trigonal planar ($S_3^{TP}$) (at $\epsilon_{\tilde{LL}} = 6.0$), (C) square planar ($S_4^{SP}$) (at $\epsilon_{\tilde{LL}} = 5.0$), (D) tetrahedral ($S_4^{TH}$) (at $\epsilon_{\tilde{LL}} = 5.0$), (E) trigonal bipyramid (S_5^{TBP}) (at $\epsilon_{\tilde{LL}} = 4.3$), and (F) octahedral ($S_6^{OCT}$) (at $\epsilon_{\tilde{LL}} = 3.8$).

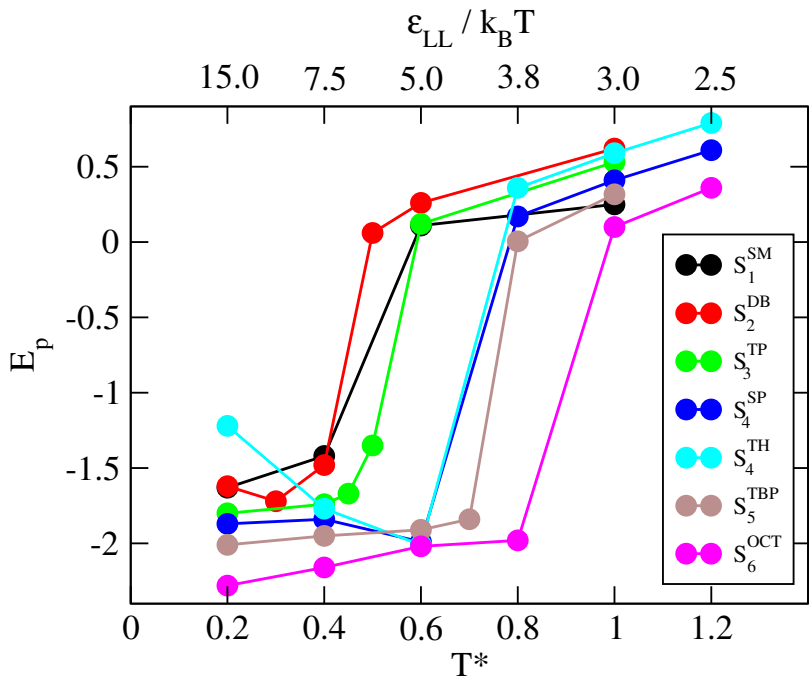

FIG. S2 Averaged potential energy per particle (E_p) vs. reduced temperature (T^*) for all types of lobed particles. The $\epsilon\tilde{_{LL}}$ (ϵ_{LL}/k_BT) values corresponding to each T^* are highlighted in the mirror-image x-axis at the top of the plot. In each case, we observed a sharp change in the E_p values when the lobed particles undergo transitions from disordered states to self-assembled states. This plot shows that with the increase in the number of lobes, the lobed particles self-assemble at lower $\epsilon\tilde{_{LL}}$ or at higher T^*.

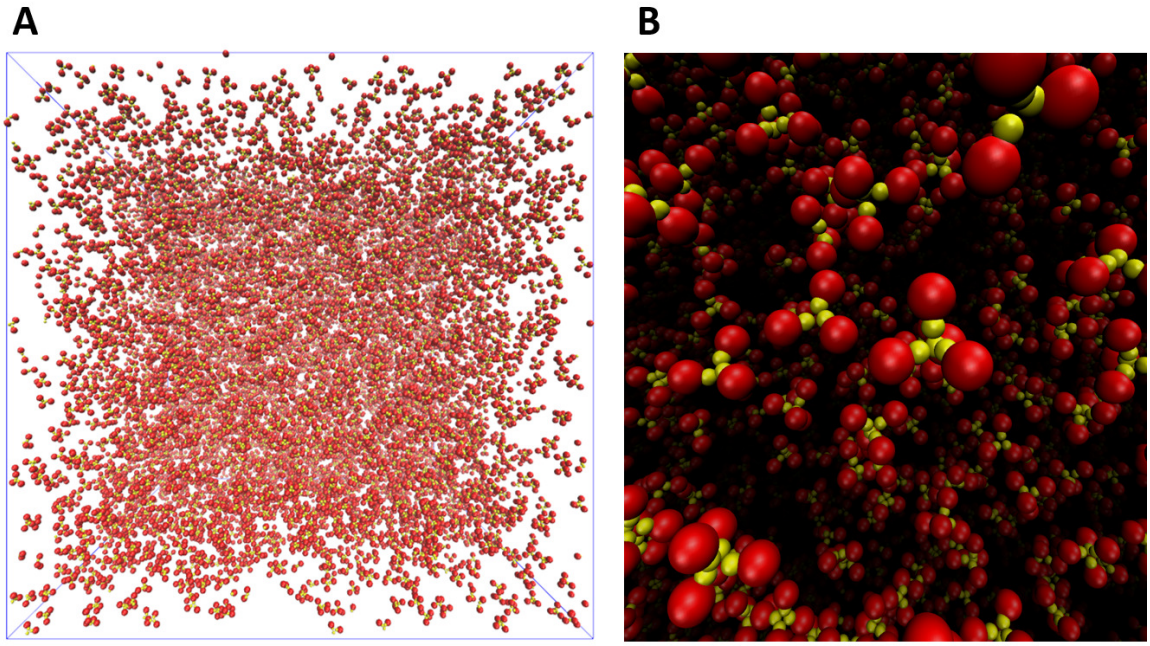

FIG. S3 (A) A snapshot of the simulation domain for the S_1^{SM} building blocks at $\tilde{\epsilon}_{LL} = 15.0$ and (B) A zoomed-view of the simulation domain showing the trigonal planar and tetrahedral clusters.

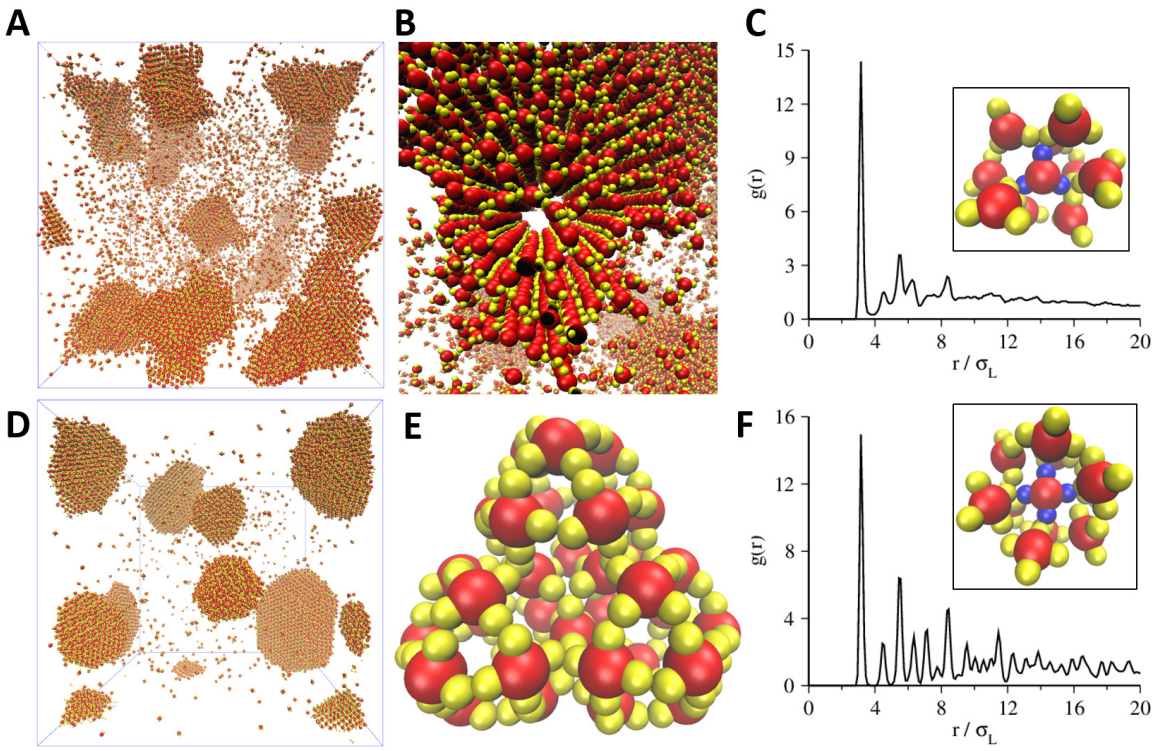

FIG. S4 Results obtained from simulations starting with different initial configurations for (A,B,C) trigonal planar (S_3^{TP}), and (D, E, F) for square planar building blocks (S_4^{SP}). (A) A snapshot of the simulation domain highlighting self-assembly for the S_3^{TP} particles at $\tilde{\epsilon}_{LL} = 6.0$; (B) A zoomed view of the simulation domain showing the formation of tubes; (C) Radial distribution function calculated for the seed pairs and the first coordination shell (inset); (D) A snapshot of the simulation domain highlighting self-assembly for the S_4^{SP} particles at $\tilde{\epsilon}_{LL} = 5.0$; (E) Clathrate-like structures formed by the self-assembly of S_4^{SP} lobed particles; (F) Radial distribution function calculated for the seed pairs showing the presence of long range order and indicating the formation of crystalline structures, where the first coordination shell is also highlighted (inset). In panels C and F, the lobes of the central particles with respect to which the first coordination shells were measured are highlighted in blue.

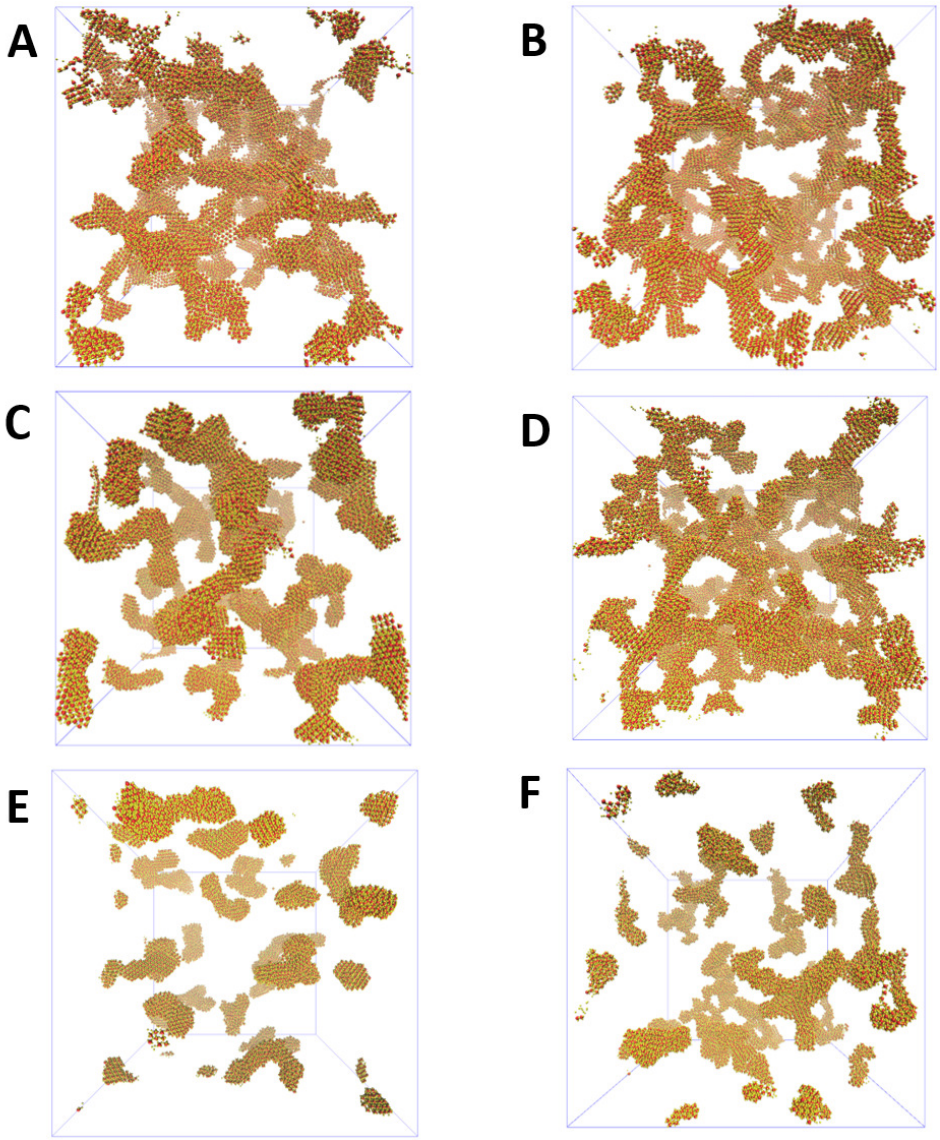

FIG. S5 Snapshots highlighting self-assembled structures in simulation domains corresponding to various types of lobed particles: (A) S_4^{SP} (at $\tilde{\epsilon}_{LL} = 7.5$), (B) S_4^{TH} (at $\tilde{\epsilon}_{LL} = 7.5$), (C) S_5^{TBP} (at $\tilde{\epsilon}_{LL} = 5.0$), (D) S_5^{TBP} (at $\tilde{\epsilon}_{LL} = 7.5$), (E) S_6^{OCT} (at $\tilde{\epsilon}_{LL} = 5.0$), and (F) S_6^{OCT} (at $\tilde{\epsilon}_{LL} = 7.5$).

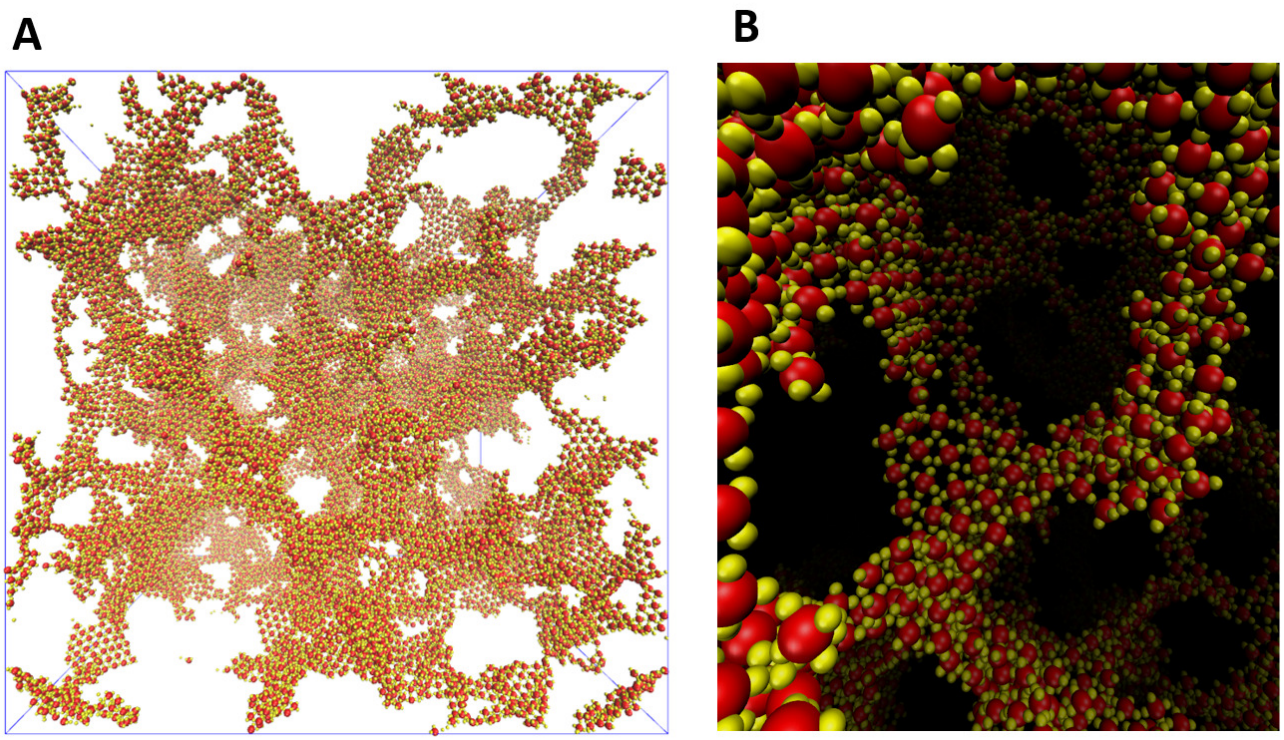

FIG. S6 (A) A snapshot of the simulation domain for S_4^{SP} particles showing self-assembly at $\tilde{\epsilon}_{LL} = 15.0$; (B) A zoomed view of the simulation domain showing the formation of two-dimensional sheets.

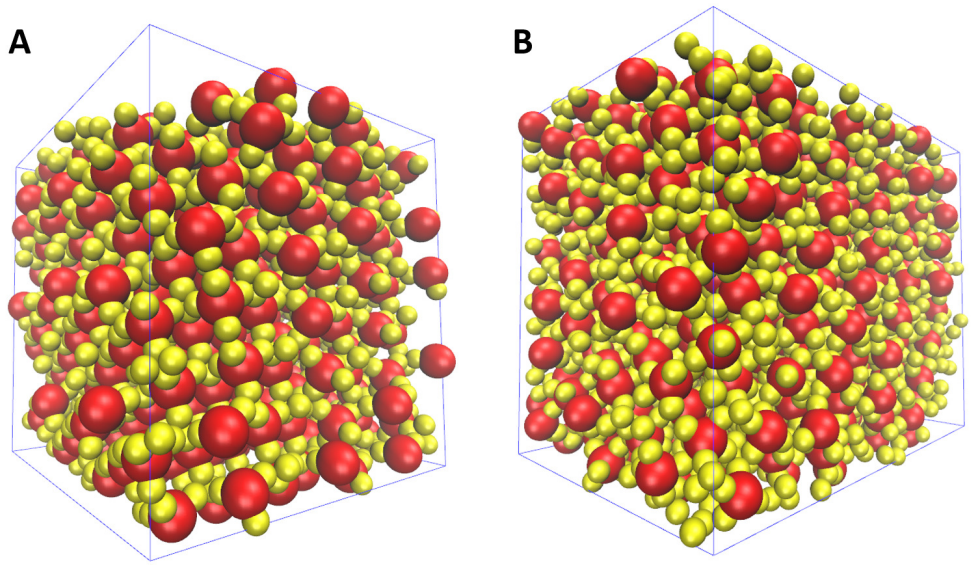

FIG. S7 Snapshots of example cuboids used to calculate pore-size distributions in self-assembled structures obtained from (A) S_4^{TH} and (B) S_5^{TBP} lobed particles.

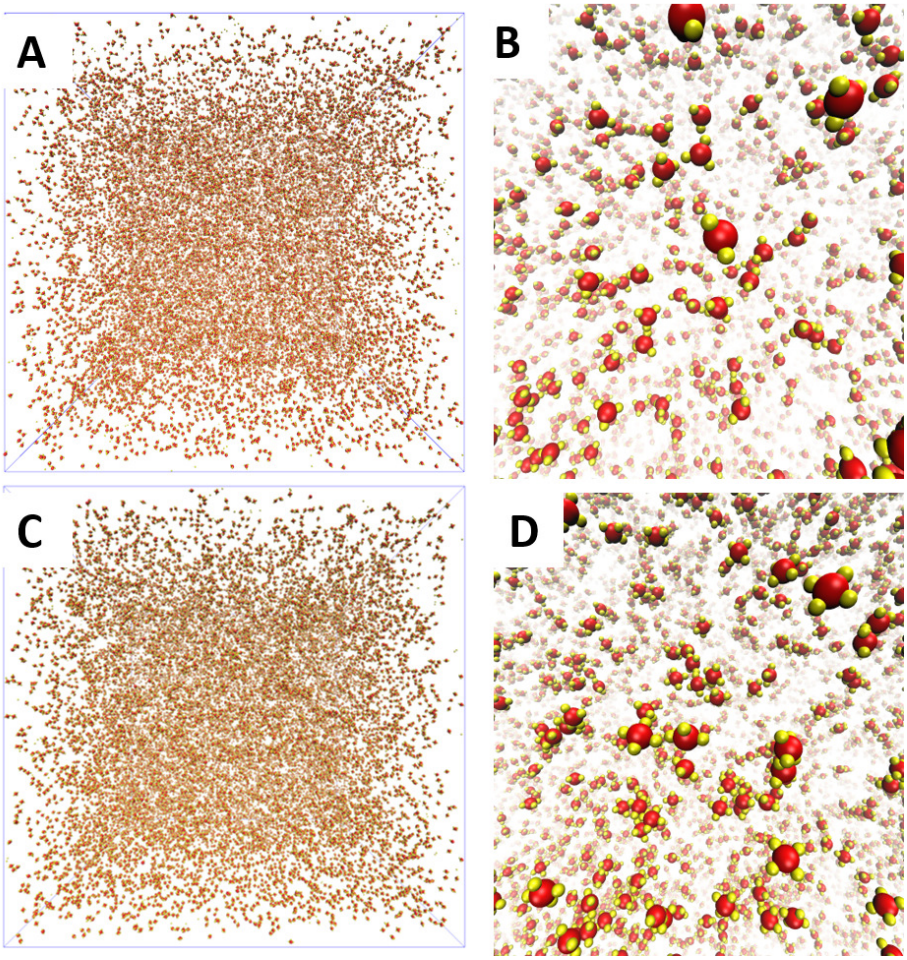

FIG. S8 Simulation domains (A and C) and their zoomed views (B and D) are shown for (A and B) trigonal planar (S_3^{TP}) (at $\tilde{\epsilon}_{LL} = 6.0$) and (C and D) for square planar (S_4^{SP}) (at $\tilde{\epsilon}_{LL} = 5.0$) particles at a volume fraction, $\phi = 0.01$. The snapshots highlight that at lower volume fractions these lobed particles do not self-assemble on simulation timescales (10^8 steps).

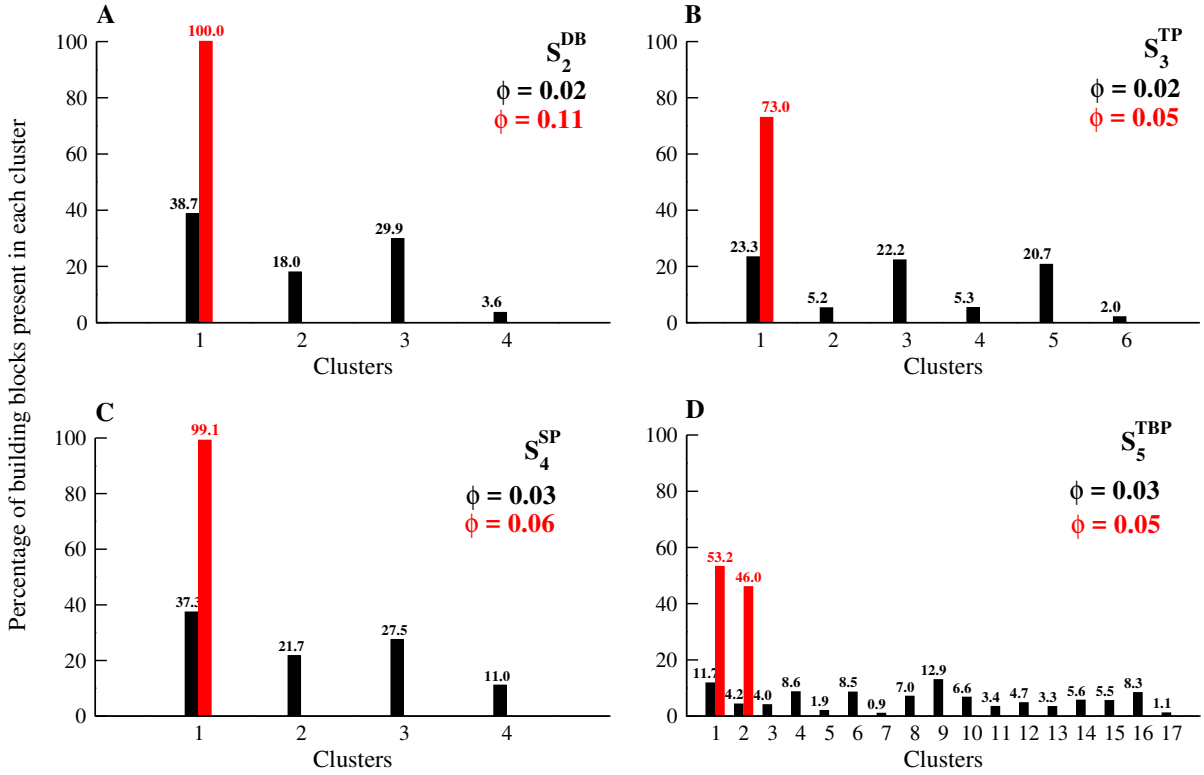

FIG. S9 The number of self-assembled clusters present at the last snapshot in various simulations and the percentage of the number of lobed particles present in each self-assembled cluster for (A) dumbbell (S_2^{DB}) (at $\tilde{\epsilon}_{LL} = 7.5$), (B) triangular planar (S_3^{TP}) (at $\tilde{\epsilon}_{LL} = 6.0$), (C) square planar ($S_4^{SP}$) (at $\tilde{\epsilon}_{LL} = 5.0$), and (D) trigonal bipyramidal (S_5^{TBP}) (at $\tilde{\epsilon}_{LL} = 4.3$) particles at different volume fractions ($\phi = 0.02$ to 0.11). These data indicate that with the increase in the volume fraction (ϕ), the number of the self-assembled clusters decreases and the size of the clusters increases. For example, (A) at $\phi = 0.02$, the dumbbell shaped (S_2^{DB}) particles form four self-assembled clusters (black bars); the percentage values of the number of particles present in each cluster has been indicated above the bars. However, at a very high volume fraction ($\phi = 0.11$), S_2^{DB} particles self-assemble into a single large self-assembled cluster (red bar) containing all the building blocks present in the simulation domain. Similar trends are observed for other building blocks.

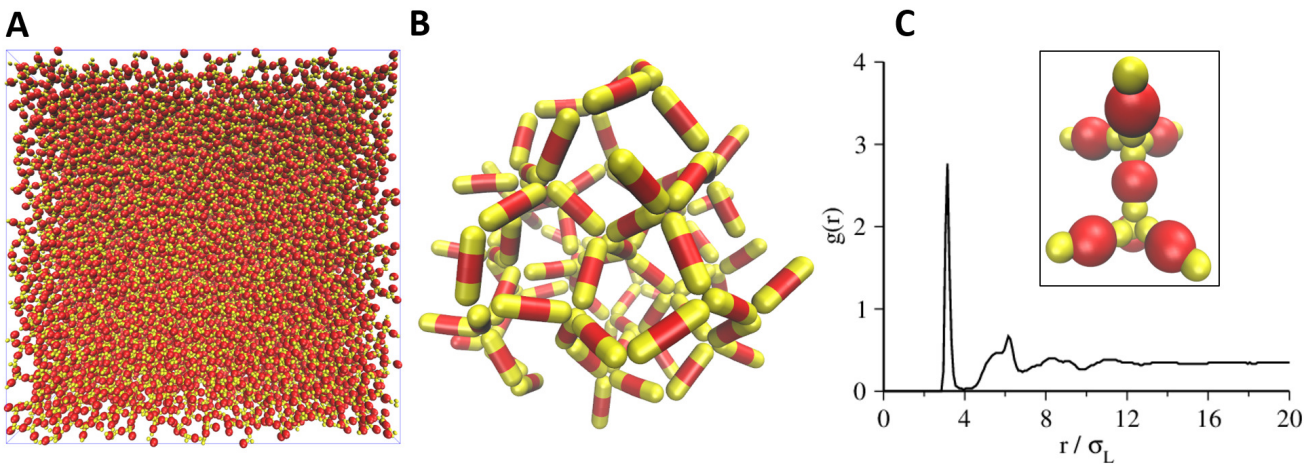

FIG. S10 Self-assembly of dumbbell (S_2^{DB}) shaped particles at a higher volume fraction, $\phi = 0.11$ at $\tilde{\epsilon}_{LL} = 7.5$. (A) Simulation domain at $t = 10^8$ highlighting that all particles self-assemble into a large cluster; (B) Local arrangement of particles showing the formation of rings; (C) Radial distribution function calculated for the seed pairs exhibiting the absence of long range order; (inset) the structure of the first coordination shell which is very similar to the first coordination shell obtained at a lower volume fraction, $\phi = 0.02$ (Fig. 2C). These findings indicate that on increasing the density of particles, local structures within the self-assembled clusters remain same although the size of the self-assembled morphology increases.